Title
Electronic-Structure Origin of Cation Disorder in Transition-Metal Oxides

Journal
Physical Review Letters, 119(17)

ISSN
0031-9007

Authors
Urban, Alexander
Abdellahi, Aziz
Dacek, Stephen
et al.

Publication Date
2017-10-27

DOI
10.1103/physrevlett.119.176402

Peer reviewed

The electronic-structure origin of cation disorder in transition-metal oxides

Alexander Urban,[1,*] Aziz Abdellahi,[2,†] Stephen Dacek,[2,†] Nongnuch Artrith,[1,†] and Gerbrand Ceder[1,3,‡]

[1] *Department of Materials Science and Engineering, University of California, Berkeley, CA, USA*
[2] *Department of Materials Science and Engineering, Massachusetts Institute of Technology, Cambridge, MA, USA.*
[3] *Materials Science Division, Lawrence Berkeley National Laboratory, Berkeley, CA, USA*

(Dated: October 17, 2017)

Cation disorder is an important design criterion for technologically relevant transition-metal (TM) oxides, such as radiation-tolerant ceramics and Li-ion battery electrodes. In this letter, we use a combination of first-principles calculations, normal mode analysis, and band-structure arguments to pinpoint a specific electronic-structure effect that influences the stability of disordered phases. We find that the electronic configuration of a TM ion determines to which extent the structural energy is affected by site distortions. This mechanism explains the stability of disordered phases with large ionic radius differences and provides a concrete guideline for the discovery of novel disordered compositions.

Substitutional disorder is a common phenomenon in transition-metal (TM) oxides and is known to affect structural and electronic properties. For example, cation disorder induces structural amorphization in $La_2Zr_2O_7$ pyrochlores [1], controls the magnetoresistance in Fe-Mo perovskites [2], and affects the critical temperature of La_2CuO_4 superconductors [3]. In rocksalt-type Li-TM oxides, cation disorder determines the Li-ion conductivity [4, 5], an important performance measure for Li-ion battery cathodes.

The technological relevance of cation-disordered oxides creates the desire to predict whether a given composition is likely to be disordered. While high-throughput first-principles computations are useful to screen specific composition spaces for stable disordered compounds [6–9], a better understanding of the origin of cation disorder might lead to simple design criteria so that time-consuming computations can be avoided.

For metallic alloys, the Hume-Rothery rules predict that species with similar electronegativity form a solid solution when their atomic radii differ no more than 15% [10, 11], but this simple heuristic does not directly translate to covalent and ionic materials such as oxides. For example, cation disorder in pyrochlores has been extensively studied [12], and while the ionic radii are an important factor for the tendency to disorder [13], species-dependent differences in the metal-oxygen bonding [14] and electronic-structure effects [6] have prevented the formulation of heuristic rules to reliably predict disorder. Likewise, B-site cation disorder in $A(B'B'')O_3$ perovskites has been linked to the similarity of the ionic radius and charge of the B' and B'' species, but these two parameters alone cannot explain all experimentally observed trends [15, 16]. On the other hand, cation-disordered Li-TM oxides with large ionic radius and charge differences are known, e.g., $LiNi_{0.5}Ti_{0.5}O_2$ [17] where the Shannon radii of Li^+, Ni^{2+}, and Ti^{4+} are 76, 69, and 61 pm, respectively [18], which seems to contradict the present understanding of the origin of cation disorder.

In an ordered structure, a TM has a single or few local high-symmetry environments, whereas a disordered structure has a large number of distinct low-symmetry environments. Hence, the ability of a TM to disorder will to some extent depend on how it can accommodate such a variety of environments [14]. We demonstrate in this letter that such an adaptability is determined by the TM's electronic structure. We show that d^0 TMs promote disorder while other d-electron configurations, especially the d^6 configuration, strongly prohibit disorder. This mechanism explains the formation of solid solutions with cation species that exhibit considerable ionic radius differences.

As a case study we focus on the Li/TM disorder in cation-disordered $LiTMO_2$ compounds, which have recently attracted interest as Li-ion battery cathode materials [5, 19–23]. The presence of Li cations with no valence electrons as one of the components simplifies the analysis by focusing on the electronic configuration of the TM.

For all first and second row TMs the ground state $LiTMO_2$ structure is either the layered $\alpha-NaFeO_2$ structure or the $\gamma-LiFeO_2$ structure with the exception of $LiMnO_2$ which forms an orthorhombic structure [8, 24]. The cation sites in these rocksalt-type Li-TM oxides are octahedral. For a large number of TMs in the $LiTMO_2$ composition we calculate the energy and relaxed atomic configuration for the ground state and the disordered structure as represented by a Special Quasi-Random Structure (SQS) [25, 26].

Structures and energies were obtained from spin-polarized density-functional theory (DFT) calculations [27–29] using the PBE functional [30, 31], PAW pseudopotentials [32] as implemented in VASP [33, 34], and k-point meshes with a density of 1000 divided by the number of atoms [35]. A Hubbard-U correction [36–39] was employed to correct the DFT self-interaction error (see Table II in the appendix). All DFT energies and

* aurban@berkeley.edu
† A. Abdellahi, S. Dacek, and N. Artrith contributed equally to this work.
‡ gceder@berkeley.edu

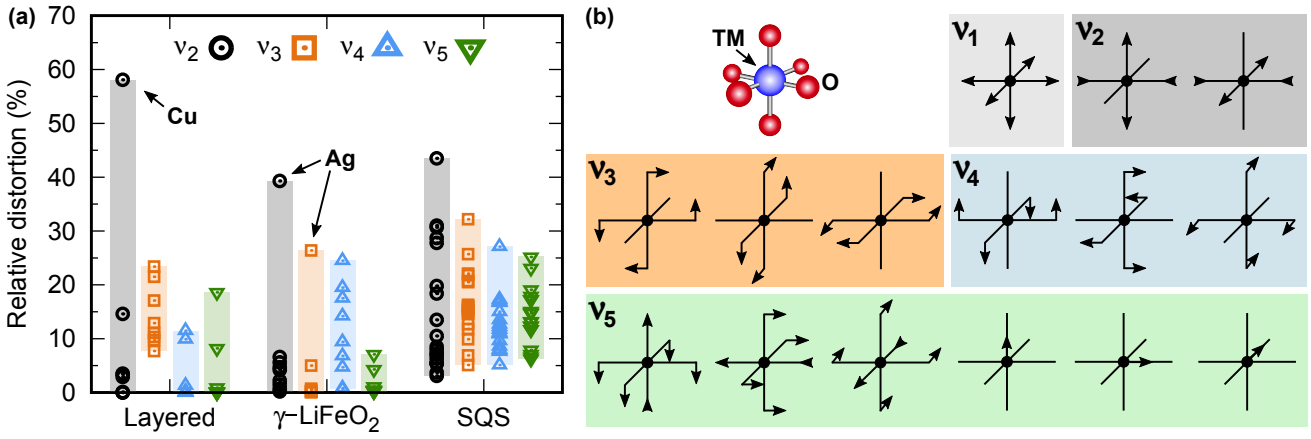

FIG. 1. **(a)** TM site distortion in the $LiTMO_2$ ground state structures (layered $\alpha-NaFeO_2$ structure and $\gamma-LiFeO_2$ structure) and in the special quasi-random structures (SQS) of all first and second-row TMs except Mn and Tc. The distortions are decomposed into contributions from different normal mode symmetry groups. The first normal mode (ν_1) corresponds to an isotropic scaling and is not considered. ν_2 is the Jahn-Teller distortion, ν_3 corresponds to bending distortions, ν_4 to twisting, and ν_5 describes the displacement of the TM from the center of the site. **(b)** Schematic of the normal modes of an octahedral TM site grouped by symmetry (rotations and translations are not shown).

atomic forces were converged to 0.05 meV per atom and 50 meV $Å^{-1}$, respectively, and the plane-wave cutoff was 520 eV.

To more directly understand the response of the TM electronic states on distortions of the local atomic environment we represent the displacement of the TM and oxygen atoms from their ideal positions in terms of the 21 normal coordinates of the octahedral MO_6 structure given in Table III. For the octahedral point group, the normal coordinates (excluding rotations and translations) belong to the five different groups ν_1 through ν_5 shown in **Fig. 1b**. The symmetric stretching mode ν_1 corresponds to an isotropic scaling and does not contribute to any distortion. The asymmetric stretching modes of type ν_2 are the modes of the Jahn–Teller (JT) distortion [40–42]. The modes of types ν_3 and ν_4 describe *bending* and *twisting*, respectively, and the modes in ν_5 describe the *displacement* of the cation from the center of the site.

The amplitude of the four symmetry-breaking normal modes around the metal cations in the two ordered ground state structures and disordered SQS are shown in **Fig. 1a** for all first- and second-row TMs except Mn and Tc. The relative distortions are given by the coefficients of the normal coordinates in the representation of the distorted octahedron D based on an ideal octahedron O, $D = O + \sum_i c_i \widetilde{Q}_i$, where $\widetilde{Q}_i$ are the normalized normal coordinates of Table III. For each group of normal coordinates, the largest coefficient c_i is plotted in **Fig. 1a** and listed in Table IV. As seen in **Fig. 1a**, the site distortions in most of the ordered layered and $\gamma-LiFeO_2$ structures range from 0 to 25% with the exception of $LiCuO_2$ (layered) and $LiAgO_2$ ($\gamma-LiFeO_2$ structure) which exhibit strong site distortions of type ν_2 because of the preference of d^8 Cu^{3+} and Ag^{3+} for square planar coordination. Further, the other ordered compounds exhibit no or only minor distortions ($< 5\%$) in the JT mode (ν_2) and the TM-displacement mode (ν_5). Contributions of the TM-displacement mode (ν_5) are only significant for the second-row TMs Nb, Mo, Ru, and Ag.

The situation is different for the SQS, in which all four types of distortions are present for all of the TMs. In addition, the magnitude of the distortions is on average greater, and the contribution of the JT mode is greater than 5% for most of the TMs. Interestingly, the amplitude of the TM-displacement mode ν_5 is also between 5% and 25% in each SQS. Hence, even cations that reside in nearly undistorted sites in their ground-state structure, e.g., (d^6) Co^{3+} and Rh^{3+}, will be subject to site distortions in a cation-disordered structure.

To interpret the effect of these site distortions on the energy of the disordered phase we consider the band-sum expression of the total energy [43–45], $U = E_{\text{band}} + \mathcal{D}$ with $E_{\text{band}} = \sum_i^{\text{occ.}} \varepsilon_i$, where ε_i are the eigenvalues of the Kohn–Sham single-electron Hamiltonian (i.e., the energies of the electronic eigenstates), and the sum over the eigenvalues of all occupied electronic states is the *band energy* E_{band}. The term $\mathcal{D}$ contains a *double-counting* correction, *electrostatics*, and contributions from the *exchange–correlation* functional, and it is mostly determined by pairwise interactions [43]. E_{band} captures the distance and angle-dependent change of the electronic states with the local structural environment [43]. Hence, to understand the energy trends in disordered structures we ought to analyze the response of E_{band} on site distortions.

We seek a qualitative picture of band-energy trends for general TM oxides rather than quantitative energies for select compositions (as these can be obtained directly from DFT), so that a simple tight-binding (TB) model of the electronic structure is most appropriate. As such, we construct a model Hamiltonian for an octahedral TM site based on the oxygen p and TM d hydrogen-like atomic

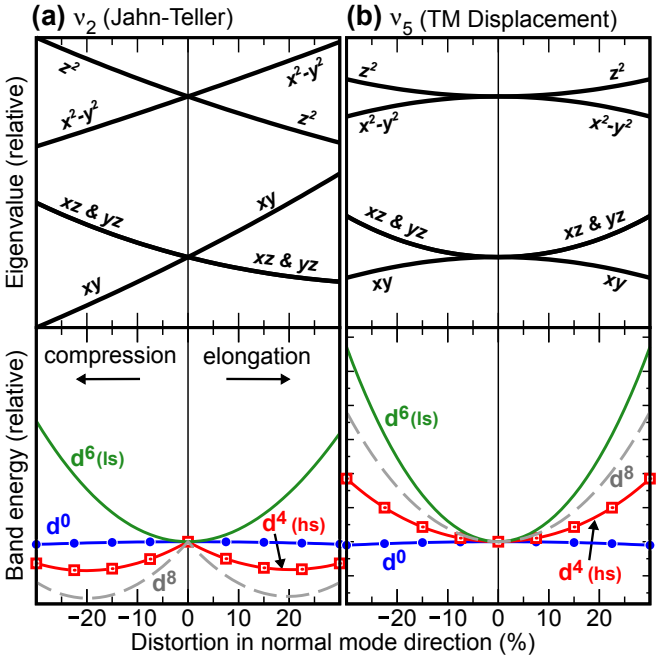

FIG. 2. Change of the electronic states (top) and the band energy (bottom) upon distortion of an octahedral TM site in the direction of **(a)** the Jahn–Teller mode (ν_2) and **(b)** the TM-displacement mode (ν_5). The band energies for four electronic configurations are shown: d^0 (blue circles), d^4 high spin (hs, red squares), d^6 low spin (ls, green line), and d^8 (gray dashed line). The energies shown in panel **(a)** are based on the conventional Jahn–Teller mode (compression/elongation in z direction) which is a linear combination of the normal coordinates of type ν_2 shown in Fig. 1b. The energy and distortion scales are equal for both normal modes. The labels in the top panels indicate the TM d orbitals that contribute most for distortions along the Cartesian z direction.

orbitals in the spirit of the extended Hückel method [46], $H_{ij} = K \frac{H_{ii}+H_{jj}}{2} S_{ij}$, where $S_{ij} = \int \phi_i(r)\phi_j(r)\,\mathrm{d}r$ is the overlap of orbitals ϕ_i and ϕ_j, $K = 1.75$ is the Wolfsberg–Helmholtz constant [46, 47], and the diagonal Hamilton matrix elements H_{ii} are the ionization potentials (IP) of the oxygen p and TM d valence states. The angular dependence of the overlap integrals is obtained from the tables by Slater and Koster [48] for reference integrals with appropriate radial symmetry (see section A in the appendix).

Note that the actual choice of the (TM-species dependent) IPs only affects the absolute energy of the electronic states ε_i but not the relative change with different distortions, so for the present discussion we only require that the oxygen p level lies lower in energy than the TM d level. Thus, the choice made for the IPs does not limit the generality of the trends discussed in the following.

Figure 2 shows the change of the electronic states and of E_{band} that results from distortions in the directions of the JT mode (ν_2) and the TM-displacement mode (ν_5) predicted by the TB model. The impact of bending (ν_3) and twisting (ν_4) distortions on E_{band} (Fig. 8) is small compared to the JT (ν_2) and displacement (ν_5) modes. Unlike the bending and twisting modes, the JT distortion and the TM displacement directly affect the TM-O bond length, explaining the stronger effect of these two modes on the energy levels.

Only the five electronic states corresponding to the TM d orbitals are shown in **Fig. 2**, i.e., the two e_g and three t_{2g} states in the ideal octahedral crystal field, as the dependence of the lower-lying states on the site distortions is negligible in comparison. The band energies for four d-electron configurations, d^0, d^4 (high spin), d^6 (low spin), and d^8 are shown in **Fig. 2**, and the remaining d-electron configurations can be found in Fig. 8. Note that E_{band} also contains contributions from the lower lying states.

Note that, while the covalent character of the TM-O bond varies with the TM species, the formal TM valence state in oxides usually corresponds to the correct d-electron count [49].

As seen in **Fig. 2**, distortions of the TM site in either JT or TM-displacement mode lower the symmetry such that the degenerate e_g and t_{2g} levels split. In the case of the JT mode, the energy of the electronic states changes approximately linearly, whereas TM displacement only gives rise to quadratic and higher-order changes. As a consequence, for TM displacements with amplitudes <5%, the relative change of the electronic states is small compared to the effect of a JT distortion with a comparable amplitude. However, for distortions with amplitudes of ≥10%, the magnitude of the energy change resulting from both normal modes is comparable.

The same general trend is seen in the band energies (**Fig. 2**), as the JT distortion results in a linear change of E_{band} for some d-electron configurations while the effect of the TM displacement is at most quadratic. The net energy change for TM displacements with amplitudes >10% is, nevertheless, larger than for JT distortions for most d-electron counts. JT distortions can increase or reduce E_{band} depending on the electronic configuration of the cation. TM displacements result in a steep increase of E_{band} for TMs with more than four valence d electrons and slightly stabilize d^1 and d^2 TMs (Fig. 8). Note that distortions in either JT or TM-displacement mode result in a strong increase of E_{band} for d^6 (low spin) and d^{10} configurations. Finally, in the absence of t_{2g} and e_g electrons, i.e., for the d^0 configuration, E_{band} solely depends on the lower-lying oxygen-dominated orbitals that are always occupied. As a result, d^0 TMs are least sensitive with respect to TM site distortions, and the variation of E_{band} is only minor.

A key conclusion of the original paper by Jahn and Teller [40] is that, to first order, only distortions of type ν_2 can affect the electronic energy. Our results are fully consistent with the JT theorem, as the TM-displacement mode (ν_5) only brings about at most second order changes of E_{band}. When the TM ion is displaced from the center of its octahedral site, one TM-O bond is elongated and a second TM-O bond is compressed, and only the difference of both effects is seen in E_{band}.

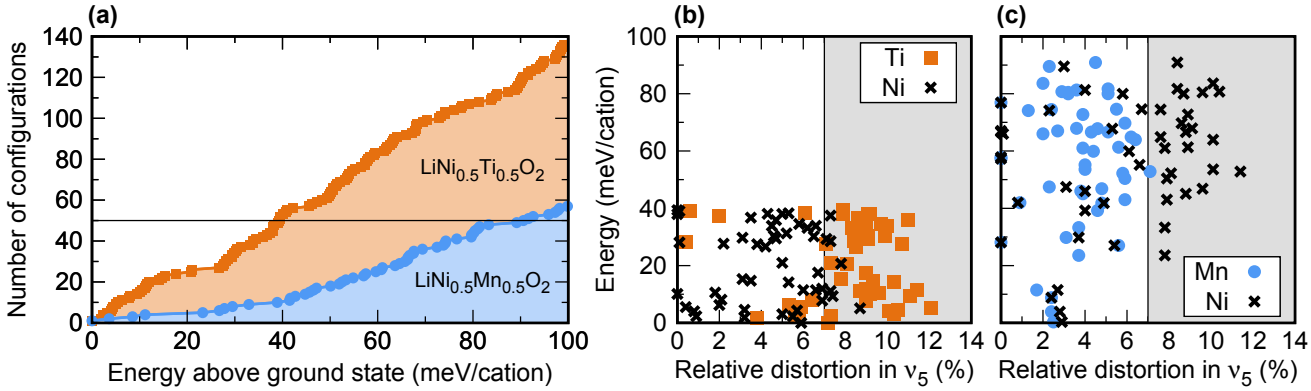

FIG. 3. **(a)** Number of $LiNi_{0.5}Ti_{0.5}O_2$ and $LiNi_{0.5}Mn_{0.5}O_2$ configurations within a 100 meV/cation from the ground state out of 469 distinct configurations with up to four formula units. **(b)** Energy per cation and TM site distortion of the 50 most stable **(b)** $LiNi_{0.5}Ti_{0.5}O_2$ and **(c)** $LiNi_{0.5}Mn_{0.5}O_2$ configurations. Only TM-displacement (ν_5) distortions are considered.

Most importantly, here we find that the second-order contributions to the band energy by the TM displacement are not negligible for the large distortions that occur in cation-disordered Li-TM oxides with amplitudes between 5 and 25% (**Fig. 1**). Additionally, from the band energies in **Fig. 2** it is obvious that not only JT active TMs are affected by site distortions, as significant energy contributions occur from distortions for any TM ion with more than zero d electrons. Since only the band energy of d^0 TMs is insensitive with respect to distortions, we conclude that d^0 TMs tolerate disordered phases even for relatively large ionic radius differences.

As seen in Fig. 9, the DFT band energies of actual d^0, d^6, and d^8 Li-TM oxides ($LiYO_2$, $LiRhO_2$, and $LiAgO_2$) follow precisely the trend predicted by the TB model for TM-displacement distortions.

TABLE I. Cation-disordered $Li_{1+x}TM_{1-x}O_2$ made by conventional solid-state synthesis. $Li_{1.211}Mo_{0.467}Cr_{0.3}O_2$, forms in the layered ($\alpha-NaFeO_2$) structure and converts to the disordered (NaCl) structure upon Li extraction and simultaneous oxidation of Mo^{5+} to Mo^{6+} [5]. The other materials form directly in the disordered rocksalt structure. d^0 TM cations are highlighted in bold font.

Composition	**TM Cations**
$LiMO_2$ (M = Ti, Fe) [24]	Ti^{3+}, Fe^{3+}
$Li_{1+x}V_2O_5$ [50]	V^{3+}, $\mathbf{V^{5+}}$
$LiM_{0.5}Ti_{0.5}O_2$ (M = Fe, Ni) [17, 51]	M^{2+}, $\mathbf{Ti^{4+}}$
$Li_{1.211}Mo_{0.467}Cr_{0.3}O_2$ [5] [a]	Mo^{5+}, Cr^{3+}
$Li_{1.25}Nb_{0.25}Mn_{0.5}O_2$ [19]	$\mathbf{Nb^{5+}}$, Mn^{3+}
$Li_{1.3}Nb_{0.3+x}M_{0.4-x}O_2$ (M = Mn, Fe, Co, Ni) [20]	$\mathbf{Nb^{5+}}$, M^{3+}
$Li_{1+x}Ti_{2x}Fe_{1-3x}O_2$ [21]	$\mathbf{Ti^{4+}}$, Fe^{3+}
$Li_{1.6-4x}Mo_{0.4-x}Ni_{5x}O_2$ [22]	$\mathbf{Mo^{6+}}$, Ni^{2+}
$Li_{1.3}Nb_{0.3}V_{0.4}O_2$ [23]	$\mathbf{Nb^{5+}}$, V^{3+}
$LiCo_{0.5}Zr_{0.5}O_2$ [8]	Co^{2+}, $\mathbf{Zr^{4+}}$

[a] Forms in layered structure but disorders upon Li extraction.

Table I lists published cation-disordered Li-TM oxides that were made by conventional solid-state synthesis [5, 8, 17, 19–24, 50, 51]. Indeed, most of the compositions contain one TM species in a formal valence state corresponding to the d^0 electronic configuration: Ti^{4+}, V^{5+}, Zr^{4+}, Nb^{5+}, or Mo^{6+}. The Li-Mo-Cr oxide of reference 5 forms in the layered structure but becomes cation disordered when Li is extracted and Mo^{5+} is oxidized to d^0 Mo^{6+}. The only cation-disordered compositions that do not contain d^0 TM species are stoichiometric $LiTiO_2$ (d^1 Ti^{3+}) and $LiFeO_2$ (d^5 Fe^{3+}) [24]. In the case of $LiFeO_2$, calorimetry measurements showed that the disordered $\alpha-LiFeO_2$ phase is in fact significantly higher (∼90 meV) in energy than the ordered $\gamma-LiFeO_2$ ground state [52], and the formation of the α-phase during synthesis has been attributed to kinetic reasons [52]. A similar mechanism might be responsible for the stabilization of cation-disordered $LiTiO_2$. Hence, the literature supports our hypothesis that d^0 cations promote cation disorder.

Finally, to understand how the presence of d^0 cations within a composition with several TM species can stabilize disordered structures, we systematically enumerated atomic configurations of $LiNi_{0.5}Mn_{0.5}O_2$, which is known to form a layered ground-state structure [53], and $LiNi_{0.5}Ti_{0.5}O_2$, which is cation disordered at typical synthesis temperatures [17]. For both compositions, the DFT energies of 469 symmetrically distinct atomic configurations with up to 8 cation sites were computed. **Figure 3a** shows the number of atomic configurations within an energy range of 100 meV/cation above the ground state for both oxides. As seen in the figure, the number of configurations within this energy interval is far greater for $LiNi_{0.5}Ti_{0.5}O_2$ (136 configuration) than for $LiNi_{0.5}Mn_{0.5}O_2$ (57 configurations). This means, for the Ti-containing composition more atomic orderings are thermally accessible at synthesis conditions. The origin of this very different energetic behavior becomes obvious when the TM site distortions are considered: **Figure 3b and c** show the TM-displacement distortions in the 50 most stable configurations of both materials. As seen in the figure,

the d^0 Ti^{4+} cations accommodate large site distortions allowing the Ni^{2+} sites to remain close to their preferred geometry. Since d^0 cations are less sensitive with respect to site distortions, the energy of these 50 configurations is within 40 meV/cation from the computational ground state. In contrast, the energy of the $LiNi_{0.5}Mn_{0.5}O_2$ configurations increases rapidly with the relative distortion of the d^8 Ni^{2+} and d^3 Mn^{4+} sites. Note that some distortion of the Ni and Mn sites is tolerable, as the band energy increases quadratically with the amplitude of ν_5 (**Fig. 2b**). Hence, not only do d^0 cations have a low energy penalty in distorted sites, their flexibility to distort allows the other TM cations to minimize their distortions.

In conclusion, we identified a specific electronic-structure effect that is responsible for the stabilization of cation-disordered phases in lithium-transition-metal oxides with large cation size differences. We showed that the strong transition-metal site distortions that occur when these compositions disorder give rise to significant second-order energy contributions. As a consequence, d^6 transition metals are strongly destabilized in cation-disordered phases, whereas d^0 transition metals can tolerate such distortions with very low energy cost. Owing to this tolerance, d^0 species can absorb site distortions in mixed compositions, even when the cation sizes differ significantly. At the example of technologically relevant lithium transition-metal oxides, we show that this insight can function as a concrete guideline for the design of novel cation-disordered compositions. While our numerical data focused on lithium-transition-metal oxides, we believe that the specific mechanism presented here by which disorder comes at lower energy cost when the TM can accommodate the distorted site more easily, will be more generally applicable to other oxides with octahedral cations.

ACKNOWLEDGMENTS

This work was supported by the Robert Bosch Corporation and by Umicore Specialty Oxides and Chemicals and by the Assistant Secretary for Energy Efficiency and Renewable Energy, Office of Vehicle Technologies of the U.S. Department of Energy under contract no. DE-AC02–05CH11231, subcontract no. 7056411. This work used the Extreme Science and Engineering Discovery Environment (XSEDE), which is supported by National Science Foundation grant number ACI-1053575. In addition, resources of the National Energy Research Scientific Computing Center, a DOE Office of Science User Facility supported by the Office of Science of the U.S. Department of Energy under Contract No. DE-AC02-05CH11231, are gratefully acknowledged.

[1] A. Chartier, C. Meis, J.-P. Crocombette, W. J. Weber, and L. R. Corrales, Phys. Rev. Lett. **94**, 025505 (2005).
[2] M. García-Hernández, J. L. Martínez, M. J. Martínez-Lope, M. T. Casais, and J. A. Alonso, Phys. Rev. Lett. **86**, 2443 (2001).
[3] J. P. Attfield, A. L. Kharlanov, and J. A. McAllister, Nature **394**, 157 (1998).
[4] A. Urban, J. Lee, and G. Ceder, Adv. Energy Mater. **4**, 1400478 (2014).
[5] J. Lee, A. Urban, X. Li, D. Su, G. Hautier, and G. Ceder, Science **343**, 519 (2014).
[6] C. Jiang, C. R. Stanek, K. E. Sickafus, and B. P. Uberuaga, Phys. Rev. B **79**, 104203 (2009).
[7] C. M. Rost, E. Sachet, T. Borman, A. Moballegh, E. C. Dickey, D. Hou, J. L. Jones, S. Curtarolo, and J.-P. Maria, Nat. Commun. **6**, 8485 (2015).
[8] A. Urban, I. Matts, A. Abdellahi, and G. Ceder, Adv. Energy Mater. **6**, 1600488 (2016).
[9] K. Yang, C. Oses, and S. Curtarolo, Chemistry of Materials **28**, 6484 (2016).
[10] W. Hume-Rothery and H. M. Powell, Zeitschrift für Kristallographie - Crystalline Materials **91**, 23 (1935).
[11] W. B. Pearson, *A handbook of lattice spacings and structures of metals and alloys*, International series of monographs on metal physics and physical metallurgy, Vol. 4 (Elsevier, 2013).
[12] K. E. Sickafus, L. Minervini, R. W. Grimes, J. A. Valdez, M. Ishimaru, F. Li, K. J. McClellan, and T. Hartmann, Science **289**, 748 (2000).
[13] F. Brisse and O. Knop, Can. J. Chem. **46**, 859 (1968).
[14] L. Minervini, R. W. Grimes, and K. E. Sickafus, J. Am. Ceram. Soc. **83**, 1873 (2000).
[15] X. wen Zhang, Q. Wang, and B. lin Gu, J. Am. Ceram. Soc. **74**, 2846 (1991).
[16] P. Davies, H. Wu, A. Borisevich, I. Molodetsky, and L. Farber, Annu. Rev. Mater. Res. **38**, 369 (2008).
[17] L. Zhang, H. Noguchi, D. Li, T. Muta, X. Wang, M. Yoshio, and I. Taniguchi, J. Power Sources **185**, 534–541 (2008).
[18] R. D. Shannon, Acta Cryst Sect A **32**, 751 (1976).
[19] R. Wang, X. Li, L. Liu, J. Lee, D.-H. Seo, S.-H. Bo, A. Urban, and G. Ceder, Electrochem. Commun. **60**, 70–73 (2015).
[20] N. Yabuuchi, M. Takeuchi, M. Nakayama, H. Shiiba, M. Ogawa, K. Nakayama, T. Ohta, D. Endo, T. Ozaki, T. Inamasu, K. Sato, and S. Komaba, Proc. Natl. Acad. Sci. USA **112**, 7650–7655 (2015).
[21] S. L. Glazier, J. Li, J. Zhou, T. Bond, and J. R. Dahn, Chem. Mater. **27**, 7751 (2015).
[22] N. Yabuuchi, Y. Tahara, S. Komaba, S. Kitada, and Y. Kajiya, Chem. Mater. **28**, 416 (2016).
[23] N. Yabuuchi, M. Takeuchi, S. Komaba, S. Ichikawa, T. Ozaki, and T. Inamasu, Chem. Commun. **52**, 2051 (2016).
[24] T. Hewston and B. Chamberland, J. Phys. Chem. Solids **48**, 97 (1987).
[25] A. Zunger, S.-H. Wei, L. G. Ferreira, and J. E. Bernard, Phys. Rev. Lett. **65**, 353 (1990).
[26] D. Shin, A. van de Walle, Y. Wang, and Z.-K. Liu, Phys. Rev. B **76**, 144204 (2007).

[27] P. Hohenberg and W. Kohn, Phys. Rev. **136**, B864 (1964).
[28] W. Kohn and L. J. Sham, Phys. Rev. **140**, A1133 (1965).
[29] A. D. Becke, J. Chem. Phys. **140**, 18A301 (2014).
[30] J. P. Perdew, K. Burke, and M. Ernzerhof, Phys. Rev. Lett. **80**, 891 (1998).
[31] J. P. Perdew, K. Burke, and M. Ernzerhof, Phys. Rev. Lett. **78**, 1396 (1997).
[32] P. E. Blöchl, Phys. Rev. B **50**, 17953 (1994).
[33] G. Kresse and J. Furthmüller, Phys. Rev. B **54**, 11169 (1996).
[34] G. Kresse and J. Furthmüller, Comput. Mater. Sci. **6**, 15 (1996).
[35] S. P. Ong, W. D. Richards, A. Jain, G. Hautier, M. Kocher, S. Cholia, D. Gunter, V. L. Chevrier, K. A. Persson, and G. Ceder, Comput. Mater. Sci. **68**, 314 (2013).
[36] V. I. Anisimov, J. Zaanen, and O. K. Andersen, Phys. Rev. B **44**, 943 (1991).
[37] A. I. Liechtenstein, V. I. Anisimov, and J. Zaanen, Phys. Rev. B **52**, R5467 (1995).
[38] S. L. Dudarev, G. A. Botton, S. Y. Savrasov, C. J. Humphreys, and A. P. Sutton, Phys. Rev. B **57**, 1505 (1998).
[39] A. Jain, G. Hautier, C. J. Moore, S. P. Ong, C. C. Fischer, T. Mueller, K. A. Persson, and G. Ceder, Comput. Mater. Sci. **50**, 2295 (2011).
[40] H. A. Jahn and E. Teller, Proc. Roy. Soc. A **161**, 220 (1937).
[41] H. A. Jahn, Proc. Roy. Soc. A **164**, 117 (1938).
[42] J. H. V. Vleck, J. Chem. Phys. **7**, 72 (1939).
[43] W. M. C. Foulkes and R. Haydock, Phys. Rev. B **39**, 12520 (1989).
[44] J. Harris, Phys. Rev. B **31**, 1770 (1985).
[45] W. M. C. Foulkes, *Interatomic forces in solids*, Ph.D. thesis, University of Cambridge (1987).
[46] R. Hoffmann, J. Chem. Phys. **39**, 1397 (1963).
[47] M. Wolfsberg and L. Helmholz, J. Chem. Phys. **20**, 837 (1952).
[48] J. C. Slater and G. F. Koster, Phys. Rev. **94**, 1498 (1954).
[49] J. Reed and G. Ceder, Electrochem. Solid-State Lett. **5**, A145 (2002).
[50] C. Delmas, S. Brèthes, and M. Ménétrier, J. Power Sources **34**, 113 (1991).
[51] H. Shigemura, M. Tabuchi, H. Sakaebe, H. Kobayashi, and H. Kageyama, J Electrochem Soc **150**, A638 (2003).
[52] M. Wang and A. Navrotsky, J. Solid State Chem. **178**, 1230 (2005).
[53] T. Ohzuku and Y. Makimura, Chem. Lett. **30**, 744 (2001).
[54] J. C. Slater, Phys. Rev. **36**, 57 (1930).

Appendix A: Bond integrals used in the tight-binding model

Our tight-binding (TB) model assumes the usual hydrogen-like atomic orbitals $\{\phi_i\}$, i.e., each atomic orbital is the product of a radial function and a (real-valued) spherical harmonic function. Only the bonds between the transition-metal d orbitals and the oxygen p orbitals are considered. Since the atomic-orbital radial functions decay exponentially with the distance from the atomic center, the same is true for the overlap of two orbitals ϕ_i and ϕ_j

$$S_{ij} = \int \phi_i(r)\phi_j(r)\,\mathrm{d}r \tag{A1}$$

and we therefore chose the form of Slater-type orbitals [54] to describe the overlap integrals $S_{pd\sigma}$ and $S_{pd\pi}$ of the two TM-O reference bonds (**Fig. 4a**)

$$S_b(r) = Ne^{-\zeta_b r} \quad \text{with the normalization constant} \quad N = 2\,\zeta_b\sqrt{\zeta_b} \quad , \tag{A2}$$

where ζ_b is a constant that controls the exponential decay. The π bond decays faster than the σ bond, so that we chose $\zeta_{pd\pi} = 2\zeta_{pd\sigma}$ with $\zeta_{pd\sigma} = 1.32$. The overlap and bond integrals resulting from this choice are shown in **Fig. 4b**. We confirmed that all of our conclusions are robust with respect to the choice of the ζ_b ratio and are not affected if the value of $\zeta_{pd\pi}$ is varied between $1\zeta_{pd\sigma}$ and $3\zeta_{pd\sigma}$.

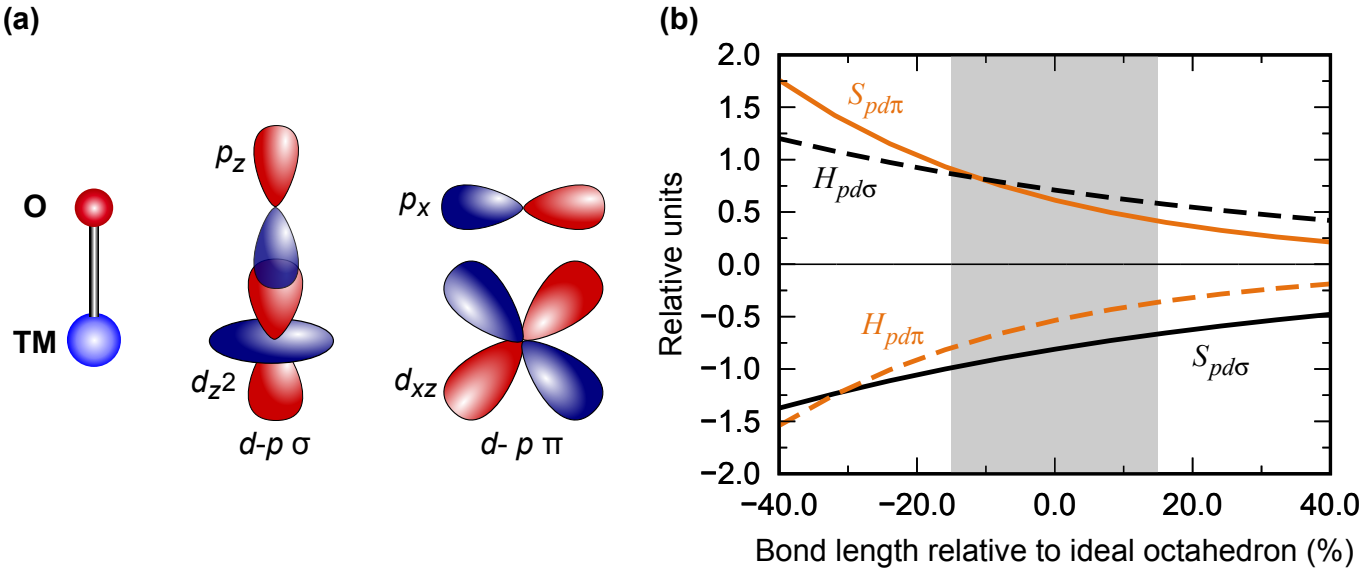

FIG. 4. **(a)** Schematic of the reference bonds between the transition-metal d and oxygen p orbitals (Cartesian z direction). All TM-O bonds for arbitrary geometries can be expressed in terms of these reference bonds following the approach by Slater and Koster [48]. **(b)** Plot of the reference overlap and bond integrals. The gray shaded region indicates the TM-O bond lengths that actually occur in the considered structures.

TABLE II. Hubbard U corrections used in DFT+U calculations. With the exception of the values for Mo, the U values are identical to those by Jain et al. [39]. The U values were fitted to measured binary formation enthalpies and are particularly well-suited for the calculation of phase stabilities.

TM	U value (eV)	TM	U value (eV)
Ag	1.50	Mn	3.90
Co	3.40	Mo	4.38
Cr	3.50	Nb	1.50
Cu	4.00	Ni	6.00
Fe	4.00	V	3.10

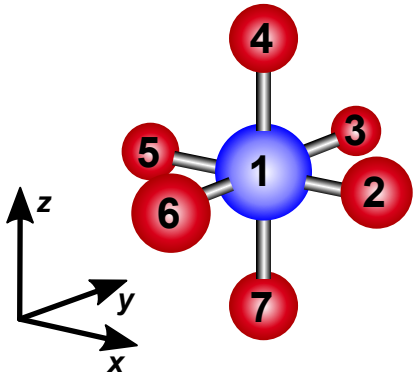

FIG. 5. Schematic showing the atom numbering convention used in Table III. Red balls indicate oxygen atoms and the blue ball indicates the TM atom.

TABLE III. Normal coordinates of the octahedral MO_6 site (not normalized or orthogonalized).

	Atom 1			**Atom 2**			**Atom 3**			**Atom 4**			**Atom 5**			**Atom 6**			**Atom 7**		
	Δx	Δy	Δz	Δx	Δy	Δz	Δx	Δy	Δz	Δx	Δy	Δz	Δx	Δy	Δz	Δx	Δy	Δz	Δx	Δy	Δz
Symmetric stretching modes																					
Q_1	0	0	0	+1	0	0	0	+1	0	0	0	+1	-1	0	0	0	-1	0	0	0	-1
Assymmetric stretching modes																					
Q_2	0	0	0	-1	0	0	0	0	0	0	0	+1	+1	0	0	0	0	0	0	0	-1
Q_3	0	0	0	-1	0	0	0	+1	0	0	0	0	+1	0	0	0	-1	0	0	0	0
Bending modes																					
Q_4	0	0	0	0	+1	0	+1	0	0	0	0	0	0	-1	0	-1	0	0	0	0	0
Q_5	0	0	0	0	0	0	0	0	-1	0	-1	0	0	0	0	0	0	+1	0	+1	0
Q_6	0	0	0	0	0	-1	0	0	0	-1	0	0	0	0	+1	0	0	0	+1	0	0
Twisting modes																					
Q_7	0	0	0	0	-1	0	0	0	0	0	+1	0	0	-1	0	0	0	0	0	+1	0
Q_8	0	0	0	0	0	-1	0	0	+1	0	0	0	0	0	-1	0	0	+1	0	0	0
Q_9	0	0	0	0	0	0	+1	0	0	-1	0	0	0	0	0	+1	0	0	-1	0	0
Displacement modes																					
Q_{10}	0	0	0	0	+1	0	0	-2	0	0	+1	0	0	+1	0	0	-2	0	0	+1	0
Q_{11}	0	0	0	0	0	+1	0	0	+1	0	0	-2	0	0	+1	0	0	+1	0	0	-2
Q_{12}	0	0	0	-2	0	0	+1	0	0	+1	0	0	-2	0	0	+1	0	0	+1	0	0
Q_{13}	0	+4	0	0	-1	0	0	0	0	0	-1	0	0	-1	0	0	0	0	0	-1	0
Q_{14}	+4	0	0	0	0	0	-1	0	0	-1	0	0	0	0	0	-1	0	0	-1	0	0
Q_{15}	0	0	-4	0	0	+1	0	0	+1	0	0	0	0	0	+1	0	0	+1	0	0	0
Translations																					
Q_{16}	+1	0	0	+1	0	0	+1	0	0	+1	0	0	+1	0	0	+1	0	0	+1	0	0
Q_{17}	0	+1	0	0	+1	0	0	+1	0	0	+1	0	0	+1	0	0	+1	0	0	+1	0
Q_{18}	0	0	+1	0	0	+1	0	0	+1	0	0	+1	0	0	+1	0	0	+1	0	0	+1
Rotations																					
Q_{19}	0	0	0	0	0	0	0	0	+1	0	-1	0	0	0	0	0	0	-1	0	+1	0
Q_{20}	0	0	0	0	0	+1	0	0	0	-1	0	0	0	0	-1	0	0	0	+1	0	0
Q_{21}	0	0	0	0	+1	0	-1	0	0	0	0	0	0	-1	0	+1	0	0	0	0	0

TABLE IV. Values of the TM site distortions visualized in Fig. 1 of the main manuscript. The orthorhombic $LiMnO_2$ structure is not shown in Fig. 1 but included here for completeness. The distortion values are the contributions of the different normal coordinates to the normal mode representation of the distorted TM sites, i.e., the expansion coefficients for each normalized normal coordinate of Table III.

TM	**Structure**	ν_2	ν_3	ν_4	ν_5	**Structure**	ν_2	ν_3	ν_4	ν_5
Ag	γ-$LiFeO_2$	0.393	0.264	0.094	0.071	SQS	0.307	0.207	0.167	0.151
Cd	γ-$LiFeO_2$	0.007	0.001	0.006	0.002	SQS	0.037	0.069	0.051	0.062
Co	α-$NaFeO_2$	0.000	0.129	0.000	0.000	SQS	0.184	0.127	0.112	0.191
Cr	α-$NaFeO_2$	0.001	0.097	0.013	0.009	SQS	0.063	0.163	0.079	0.123
Cu	α-$NaFeO_2$	0.581	0.234	0.000	0.000	SQS	0.278	0.152	0.150	0.079
Fe	γ-$LiFeO_2$	0.002	0.005	0.175	0.003	SQS	0.079	0.118	0.080	0.124
Mn	o-$LiMnO_2$	0.201	0.060	0.083	0.061	SQS	0.198	0.205	0.173	0.117
Mo	γ-$LiFeO_2$	0.015	0.050	0.068	0.043	SQS	0.054	0.161	0.109	0.117
Nb	α-$NaFeO_2$	0.035	0.111	0.099	0.186	SQS	0.072	0.159	0.135	0.172
Ni	α-$NaFeO_2$	0.146	0.103	0.002	0.002	SQS	0.135	0.155	0.117	0.066
Rh	α-$NaFeO_2$	0.000	0.171	0.000	0.001	SQS	0.310	0.218	0.127	0.179
Ru	α-$NaFeO_2$	0.034	0.215	0.115	0.082	SQS	0.435	0.322	0.170	0.231
Sc	γ-$LiFeO_2$	0.022	0.001	0.195	0.005	SQS	0.070	0.147	0.096	0.147
Ti	γ-$LiFeO_2$	0.042	0.002	0.008	0.004	SQS	0.054	0.099	0.086	0.132
V	α-$NaFeO_2$	0.029	0.077	0.001	0.001	SQS	0.085	0.148	0.109	0.148
Y	γ-$LiFeO_2$	0.047	0.007	0.245	0.011	SQS	0.105	0.221	0.168	0.173
Zn	γ-$LiFeO_2$	0.066	0.001	0.142	0.002	SQS	0.031	0.051	0.076	0.071
Zr	γ-$LiFeO_2$	0.056	0.002	0.047	0.003	SQS	0.055	0.153	0.122	0.131

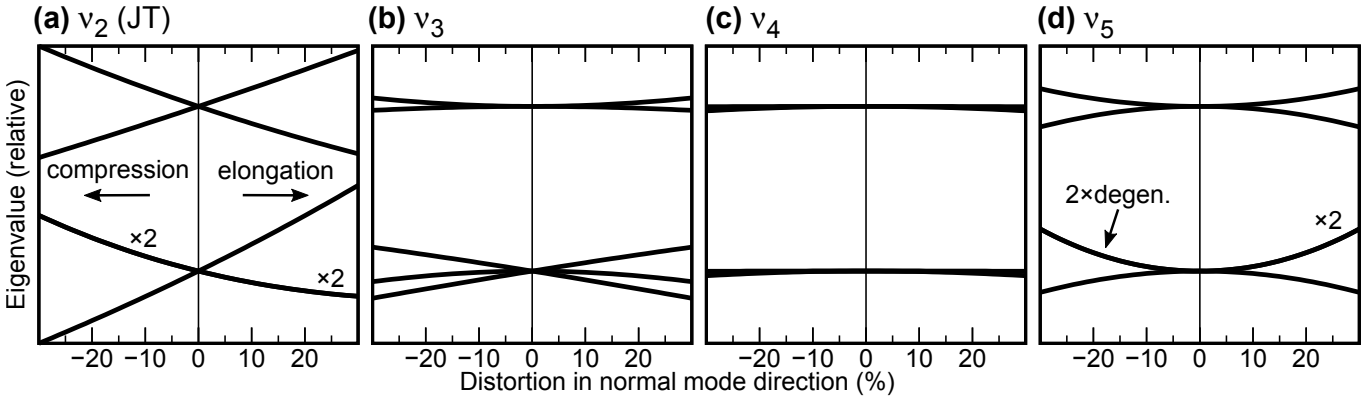

FIG. 6. Tight-binding eigenvalues for all symmetry-breaking normal modes.

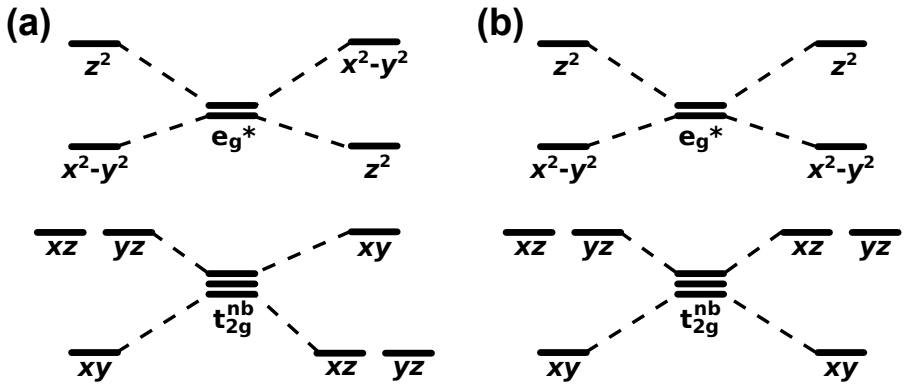

FIG. 7. Schematic of the molecular orbital level splitting on distortion in the **(a)** Jahn-Teller mode (ν_2) and **(b)** transition-metal displacement mode (ν_5). The labels refer to the transition-metal d orbital that contributes most to the state. The vertical spacing does not reflect actual energy units.

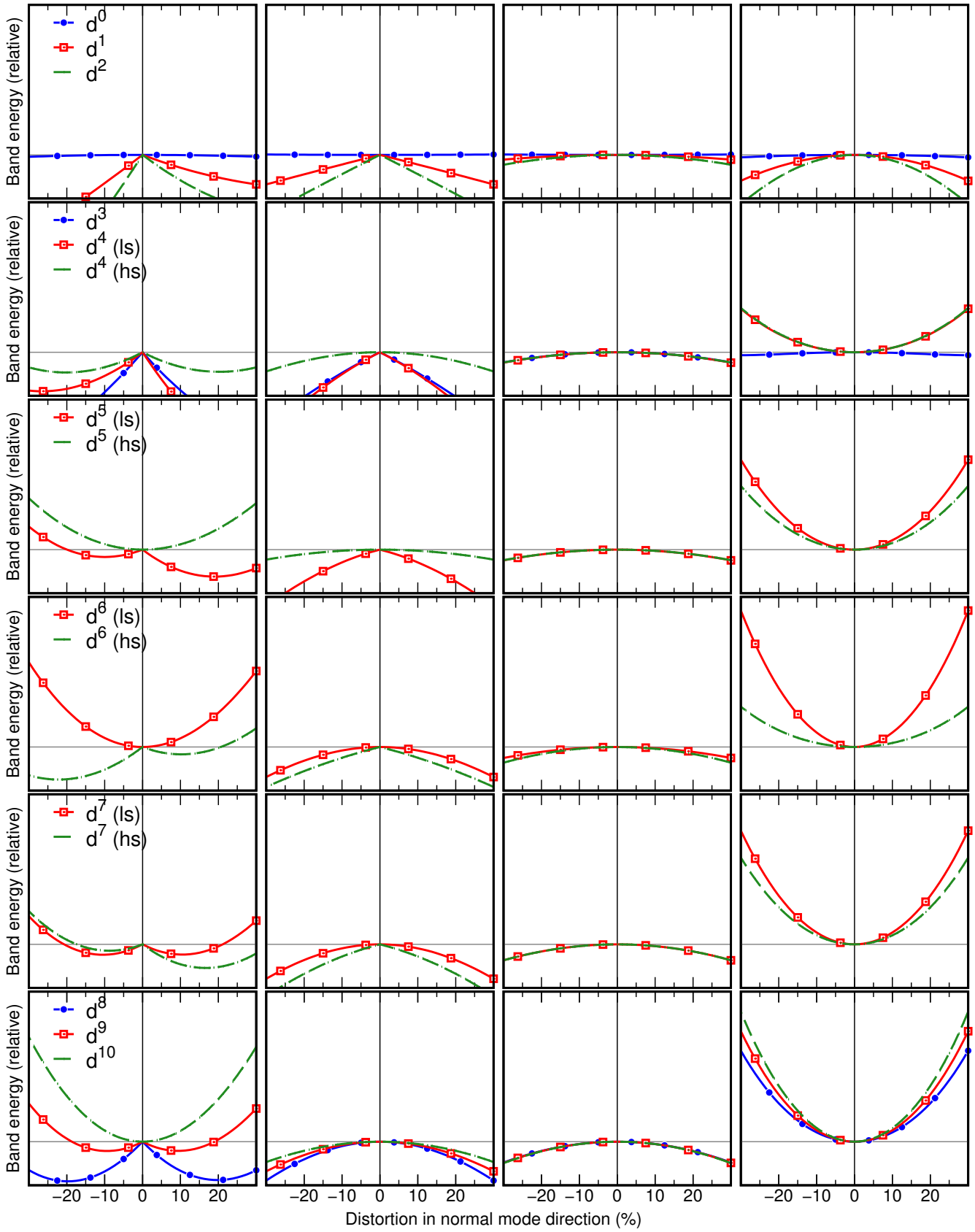

FIG. 8. Tight-binding band energies for all d-electron configurations and spin states upon distortion in the direction of the five symmetry-breaking normal modes.

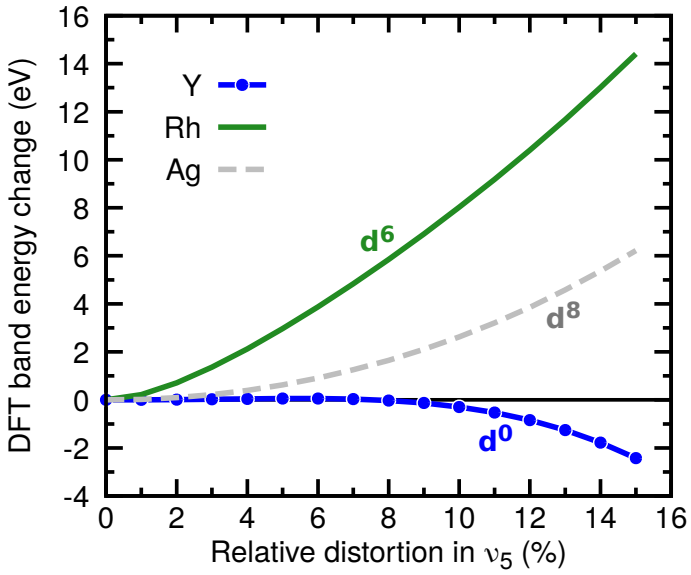

FIG. 9. Change of the density-functional theory (DFT) band energies of $LiYO_2$, $LiRhO_2$, and $LiAgO_2$ upon distortion of the transition-metal site in the TM-displacement mode (ν_5). To ensure a global energy reference, all DFT eigenvalues were calculated relative to the energy of the oxygen $2s$ states which does not significantly hybridize with the valence bands of the $4d$ TMs. The d-electron configuration of the transition metal cations is d^0 for Y^{3+}, d^6 (low-spin) for Rh^{3+}, and d^8 for Ag^{3+}. The band energies shown in the figure are one concrete example of the general band energy trends shown in Fig. 2b of the main manuscript.